Bioactive Materials 43 (2025) 564–578

Contents lists available at ScienceDirect

Bioactive Materials

journal homepage: www.keaipublishing.com/en/journals/bioactive-materials

Novel ultrathin ferrous sulfide nanosheets: Towards replacing black phosphorus in anticancer nanotheranostics

Yuan Gao [a,1], Mengyao Mu [a,1], Yiju Wei [b,1], Bowen Yan [a], Hui Liu [a], Kai Guo [c,***], Mengmeng Zhang [a], Xiaohui Dai [a], Xiao Sun [a,d,**], David Tai Leong [e,*]

[a] School of Chemistry and Pharmaceutical Engineering, Medical Science and Technology Innovation Center, Shandong First Medical University and Shandong Academy of Medical Sciences, Jinan, 250000, China
[b] School of Life Science, Shandong First Medical University and Shandong Academy of Medical Sciences, Jinan, 250117, China
[c] Department of Radiology, Shandong Provincial Hospital Affiliated to Shandong First Medical University, Jinan, 250021, China
[d] Shandong Cancer Hospital and Institute, Shandong First Medical University and Shandong Academy of Medical Sciences, Jinan, 250117, China
[e] Department of Chemical and Biomolecular Engineering, National University of Singapore, Singapore, 117585, Singapore

ARTICLE INFO

Keywords:
Biodegradable
FeS nanosheets
Black phosphorus
Synergistic ferroptosis–PTT
MRI

ABSTRACT

Biodegradable two-dimensional nanomaterials could be a significant breakthrough in the field of oncology nanotheranostic agents, which are rapidly emerging as promising candidates for tumor theranostic applications. Herein, a novel biodegradable ferrous sulfide nanosheet (FeS NS) is developed. Compared to the traditional photothermal material, black phosphorus nanosheet (BP NS), FeS demonstrates superior degradability and enhanced photothermal performance, and making it ideal for efficient photothermal therapy (PTT) of tumors. In the acidic tumor microenvironment, FeS degrades and releases H_2S, which inhibits mitochondrial respiration and ATP production. This process leads to a reduction in heat shock protein expression, lowering the resistance of tumor cells to photothermal stimulation, and improving the efficacy of PTT. The released Fe^{2+} exhibits efficient peroxidase activity, triggering ferroptosis in tumor cells. Furthermore, due to its superparamagnetic nature, FeS NSs could accumulate at the tumor site and provide a strong magnetic resonance imaging (MRI) signal for imaging-guided tumor therapy. Overall, as a promising alternative to BP, the FeS NSs are a potentially innovative nanotheranostic agent of tumors, offering a synergistic approach to ferroptosis–PTT with MRI guidance.

1. Introduction

The ultrathin structure of two-dimensional (2D) nanomaterials, such as the high specific surface area and excellent surface properties like optical, ultrasonic, magnetic response, has attracted significant research interest [1]. Biodegradable 2D nanomaterials hold promise for future cancer theranostics [2], provided they can achieve a balance between functioning in the body for an adequate period and being metabolically cleared from the body promptly. While most nanomaterials undergo some form of biodegradation, the rate and degree of degradation vary widely. Biodegradable nanomaterials undergo rapid and complete degradation, whereas non-biodegradable nanomaterials degrade slowly and incompletely. Within the body, biodegradable nanomaterials engage in a dynamic process, progressively breaking down into smaller size or ions across various organs, circulating through the bloodstream, and ultimately being either absorbed or excreted from the body [3]. For example, iron ions degraded by iron oxide in the body can be stored in certain proteins or eliminated through typical iron metabolic pathways [4]. However, non-biodegradable or slow-biodegradable 2D materials have a low clearance rate and pose various acute toxicity and long-term safety concerns. For example, the injection of nanoscale graphene oxide (GO) into mice led to acute lung injury and chronic lung fibrosis [5]. GO

Peer review under responsibility of KeAi Communications Co., Ltd.
* Corresponding author.
** Corresponding author. School of Chemistry and Pharmaceutical Engineering, Medical Science and Technology Innovation Center, Shandong First Medical University and Shandong Academy of Medical Sciences, Jinan, 250000, China.
*** Corresponding author.
E-mail addresses: kguo@sdfmu.edu.cn (K. Guo), sunxiao@sdfmu.edu.cn (X. Sun), cheltwd@nus.edu.sg (D.T. Leong).
[1] These authors contributed equally to this work.

https://doi.org/10.1016/j.bioactmat.2024.09.035
Received 18 July 2024; Received in revised form 12 September 2024; Accepted 24 September 2024
Available online 14 October 2024

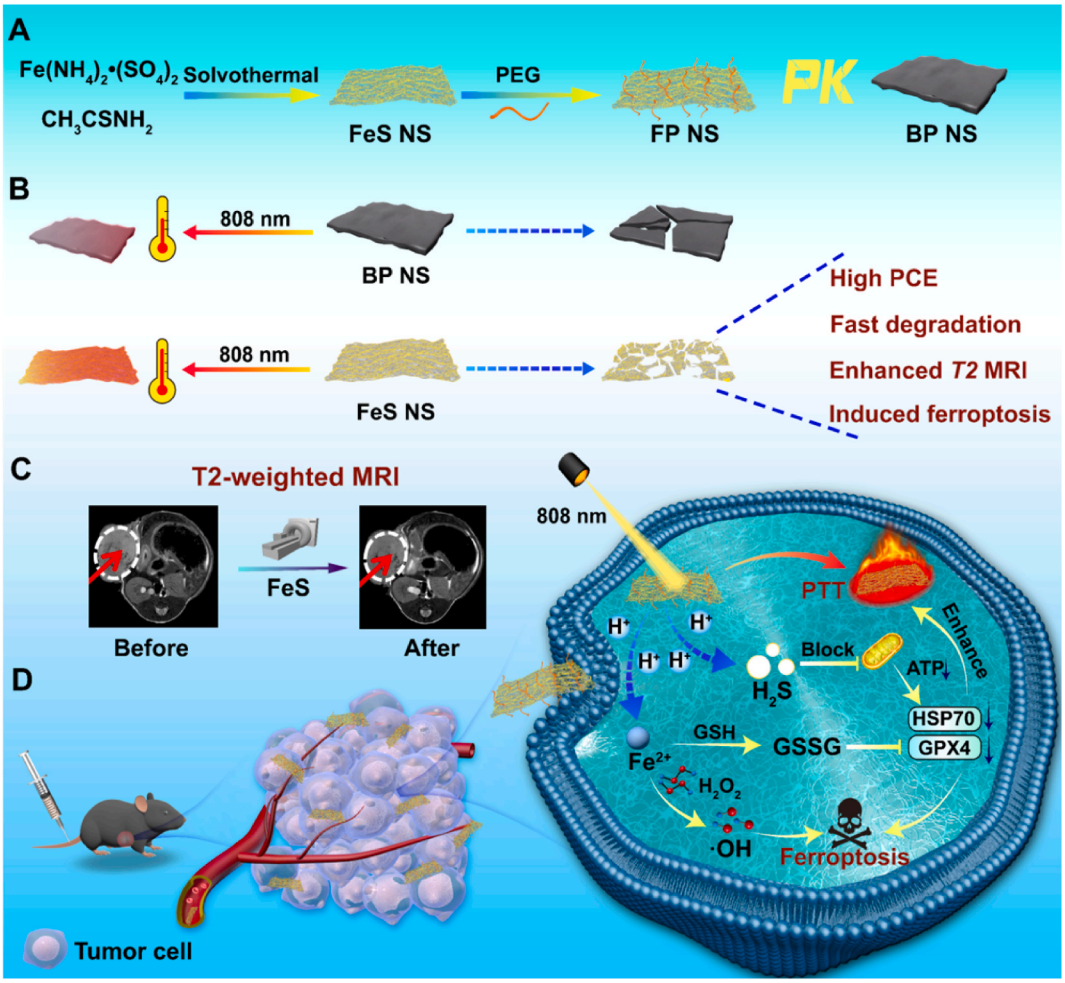

Scheme 1. Schematic illustration of (A) the detailed synthesis of FeS-PEG, (B) Superiority of FeS over BP, (C) Enhanced T2 MRI performance of FeS, and (D) Mechanism of FeS-PEG in promoting ferroptosis-enhanced PTT of tumors.

nanocolloids were found to be toxic to human skin fibroblasts at low concentrations [6]. Graphene also exhibited significant toxicity to human astrocytes [7], while MoS_2 triggered notable toxicity in Kupffer cells [8]. Hexagonal boron nitride showed cytotoxic effects in mouse trachea, human alveolar and human corneal epithelial cells [9]. Therefore, the development of biodegradable 2D nanomaterials is crucial for clinical translation and holds promising applications in the biomedical field.

In recent years, a biodegradable 2D nanomaterial, such as black phosphorus nanosheet (BP NS), have gained significant attention as promising alternatives to other 2D nanomaterials due to its excellent physical and chemical properties, which has been extensively explored and applied in multiple fields [10,11], and shown considerable potential in photothermal therapy (PTT) for tumors [12]. BP NSs are primarily composed of phosphorus, an element naturally abundant in the human body, enabling the material to degrade into non-toxic byproducts. BP NSs has become the darling material amongst all current biodegradable 2D nanomaterials for cancer nanotheranostics. However, current exfoliation-based preparation methods for BP often produce nanosheets with numerous defects [13], limited universality, low yield, and high production costs. Consistent size and morphology of nanosheets are crucial for biomedical applications, however, mechanical exfoliation methods often yield variable sizes and shapes. Additionally, BP exhibits a slow degradation rate and reduced ultraviolet absorption 1/3 after 72 h in aqueous or bodily fluid environments. After 7 days, transmission electron microscope (TEM) analysis revealed a sheet structure with blurred edges and rough surfaces, while still a relatively intact nanosheet structure [14]. Despite their potential as photothermal agents, BP NSs exhibit suboptimal photothermal efficiency and limited therapeutic efficacy due to their inherent properties and lack of functional groups for surface modification [15,16]. Therefore, developing optimized biodegradable 2D nanomaterials with improved properties remains a critical need for achieving efficient PTT in tumor therapy.

Through rational design and synthesis of nanomaterials, it is possible to integrate various clinical diagnostic and therapeutic processes into a single nanosystem which enables real-time and precise disease diagnosis and treatment [17–19]. Moreover, this approach also facilitates the monitoring of treatment efficacy, timely dosing adjustments, and ultimately better therapeutic outcomes for patients [20]. Magnetic Resonance Imaging (MRI) is a radiation-free imaging technique known for its high spatial resolution, deep tissue penetration ability and excellent soft tissue contrast, making it a valuable tool in clinical research [21]. Nanoprobes are currently being explored as potential MRI contrast agents to enhance imaging sensitivity and specificity [22,23]. However, safety concerns regarding contrast agents pose a challenge to their clinical translation. It has been reported that gadolinium-based contrast agents have been associated with nephrogenic systemic fibrosis in some patients, leading to dose reductions that can compromise imaging quality [24]. In contrast, iron-based nanomaterials offer advantages such as natural degradation mechanisms, good biocompatibility, and the potential induction of ferroptosis in cells [25]. Therefore, various iron-based nanomaterials have been extensively studied for cancer theranostics [26], due to their superparamagnetic properties, improved biocompatibility, and cost-effectiveness [27]. And the accumulation of

the released iron ions in cells leads to ferroptosis. Xie et al. developed amorphous ferrous sulfide-embedded bovine serum albumin (FeS@BSA) nanoclusters that released Fe^{2+} under acidic conditions, triggering a rapid Fenton reaction to induce cytotoxic ROS production in cancer cells and released H_2S in Huh7 cancer cells [28]. Following intravenous injection in mice, FeS@BSA aggregated at the tumor site and produced a strong MRI signal. This observation led to the development of an MRI-guided nanoplatform for tumor theranostics.

Herein, a novel biodegradable 2D ferrous sulfide nanosheets (FeS NSs) was developed and compared to BP NSs for tumor PTT. FeS NSs demonstrated higher efficiency for PTT, with superior photothermal conversion efficiency (PCE) (Schemes 1A, B). In addition to higher PCE for PTT, FeS also released H_2S in acidic tumor microenvironments, inhibiting mitochondrial respiration and ATP production, leading to reduced HSP70 expression and increased sensitivity of tumor cells to PTT. Additionally, the released Fe^{2+} exhibited potent peroxidase (POD) activity, inducing ferroptosis in tumor cells at the same time (Scheme 1D). Furthermore, FeS within the tumors generated robust MRI signals, which guided synergistic ferroptosis-PTT therapy for effective tumor elimination (Scheme 1C). Overall, FeS exhibits strong potential as a 2D photothermal nanomaterial, offering enhanced efficacy in tumor therapy compared to BP.

2. Materials and methods

2.1. Materials

Black phosphorus nanoplates dispersion was purchased from Nanjing/Jiangsu XFNANO Materials Tech Co. Ltd. $Fe(NH_4)_2{\cdot}(SO_4)_2{\cdot}6H_2O$, PEI, PEG, trisodium citrate, thioacetamide and bisBenzimide H33342 trihydrochloride (Hoechst 33342) were purchased from Aladdin Chemical Co. Ltd. (Shanghai, China). Fetal bovine serum (FBS) was purchased from Lonsera (USA). Dulbecco's modified Eagle's medium (DMEM), Phosphate-buffered saline (PBS) and penicillin-streptomycin and ATP Assay Kit were purchased from Beyotime biotechnology (Shanghai, China). FITC, BCA protein assay kit, cell lysis buffer for Western blotting, and IP, primary antibody dilution buffer and other commonly used buffers were purchased from Aladdin Chemical Co. Ltd. (Shanghai, China). Cy5.5 and WSP-1 were purchased from Shanghai Maokang Biotechnology Co. Ltd. Mitochondrial Membrane Potential Assay Kit with JC-1 was purchased from Solarbio Science & Technology Co., Ltd. (Beijing, China). BODIPY581/591-C11, SuperSignal West Pico PLUS chemiluminescent substrate was purchased from Thermo Fisher Scientific Co. (USA). GAPDH Monoclonal Antibody and GPX4 Polyclonal Antibody were purchased from Proteintech. Hsp70 Rabbit Monoclonal Antibody was purchased from Beyotime biotechnology. All chemical reagents were used directly without further purification.

2.2. Measurements

The morphology and element composition of the NSs were observed by TEM (Talos F200i) and AFM (Bruker Dimension ICON). The particle size distribution and ζ potential were measured by using a DLS detector (Malven, UK). The UV–vis spectra were performed with a UV spectrophotometer (Thermo Fisher, USA). Fourier transform infrared (FTIR) was detected by a Magna-560 spectrometer. Metal content was quantified on an ICP-OES instrument (G8018A, Agilent, USA). Cell uptake, intracellular ROS detection and H_2S detection etc. Were observed by CLSM (DMi8, Leica, Germany).

2.3. Cell culture

The DMEM medium was mixed with 10 % FBS and 1 % antibiotics (penicillin and streptomycin) for the culture of LLC and HUVEC cells. The culture condition is 37 °C in a humidified environment containing 5 % CO_2. For cell harvesting, 0.5 % w/v trypsin in PBS was used to detach from the cell culture dish and then resuspended in a fresh medium for the following usage.

2.4. Animal experiment

C57BL/6 mice (Half male and half female, 6 weeks old) were obtained from Huafukang Bioscience Co. (Beijing, China). All animal experiments are fully authorized and approved by the Experimental Animal Care Ethics Committee of Shandong First Medical University (Approval No. SDTHEC2023003137).

2.5. Synthesis of FeS nanosheets

$Fe(NH_4)_2{\cdot}(SO_4)_2$ (0.6 mmol) and trisodium citrate (0.2 mmol) were dissolved in 15 mL of ethylene glycol, and PEI (500 mg) dissolved in 5 mL ethylene glycol was added to the above solution and stirred for 120 min. Subsequently, thioacetamide and triethanolamine (2 mL) were added to the mixture and stirred for a further 5 min. Afterward, the product was transferred to a stainless-steel autoclave lined with Teflon and kept at 200 °C for 24 h. Finally, the product was collected by centrifugation.

2.6. Synthesis of FeS-PEG and BP-PEG

FeS (1 mg) or BP (1 mg) and PEG (50 mg) were dissolved in 5 mL of anhydrous ethanol (BP in deionized water) and stirred under dark conditions for 6 h at room temperature. The product was centrifuged, washed, and finally dispersed in anhydrous ethanol or deionized water.

2.7. Degradation behavior of FeS NSs

FeS NSs and BP NSs of the same mass were incubated in PBS at room temperature, and the images of the color change and the absorbance were recorded, and its extinction coefficient was calculated. $A(\lambda) = \varepsilon \times C \times L$, where A represents the absorbance, L and C represent the path-length (10 mm) and the FeS concentration (g/L), respectively. To evaluate the photothermal-enhanced degradability of FeS, FeS-dispersed aqueous suspensions (150 μg/mL) were exposed to laser irradiation with varied power. The absorbance spectra and TEM images of FeS aqueous solutions at the corresponding temperatures were collected.

2.8. In vitro cytotoxicity study

LLC cells in the logarithmic growth phase were taken and inoculated into 48-well plates (2×10^4 cells/well), and cultured in DMEM at 37 °C with 5 % CO_2 for 24 h. They were then treated with the sample with different concentrations and NIR (1.5 W/cm^2) irradiated for 5 min/well, and then cultured for 6 h. Cell survival was detected by the MTT assay. Briefly, the MTT reagent (1:5 diluted in DMEM) was added to each well and the plates were incubated for another 3.5 h. DMSO was then introduced (200 μL/well) and the plates were kept in the dark for an additional 15 min. Measurements of absorbance were subsequently completed with a microplate reader.

2.9. Biocompatibility assay

HUVEC in logarithmic growth phase were taken and inoculated in 96-well plates, and cultured in DMEM at 37 °C with 5 % CO_2. After that, the cells were treated with FP and BPP at different concentrations for 24 h. Cell survival was detected by the MTT assay.

2.10. Cell uptake

LLC cells in the logarithmic growth phase were inoculated in confocal dishes (3×10^5 cells/dish) and cultured for 24 h. Subsequently, the cells were treated with different concentrations of FP-Cy5.5 for 4 h

and then stained with Hoechst under dark conditions for 15 min. Then cells were washed twice with PBS and kept in 1 mL PBS for CLSM. LLC cells were inoculated in 6-well plates (3×10^5 cells/well) and then treated by FP-FITC for 4 h. Subsequently, flow cytometry was used for detection.

2.11. Live/dead cell staining

The *in vitro* therapeutic effect was explored with a cell viability/cytotoxicity assay kit that can label live/dead cells with calcein AM and PI probes, respectively. In short, LLC cells were inoculated in 6-well plates (4×10^5 cells/well) and cultured for 24 h. After that, the cells were treated with different conditions, 6 h later, mixed with DMEM containing AM (2 μM) and PI (4.5 μM) under dark conditions for 30 min and washed with PBS. Then cells were visualized by CLSM to observe the staining results.

2.12. Intracellular ·OH detection

Intracellular ROS production was investigated by 2,7-dichlorodihydrofluorescein diacetate (H2DCFDA). LLC cells were inoculated in confocal dishes (3×10^5 cells/dish) and incubated for 24 h. Subsequently, the cells were divided into different processing (Control, 50 μg/mL FP, 100 μg/mL FP and 100 μg/mL BPP). After 6 h, the cells were incubated with H2DCFDA (10 μM) in dark conditions for 30 min. Intracellular DCF fluorescence was observed by CLSM.

2.13. Intracellular H_2S detection

LLC cells were inoculated in a confocal dish (3×10^5 cells/dish) and cultured for 24 h. They were divided into negative control, FP and Na_2S-positive control groups for 4 h incubation respectively. After that, cells were incubated with WSP-1 probes according to the manufacturer's protocol, and the production of H_2S in the cells was observed through CLSM.

2.14. Intracellular ATP Level Evaluation

LLC cells were inoculated in 6-well plates (2×10^5 cells/well) and incubated for 24 h, then incubated with FP (80 μg/mL) for 24 h. Subsequently, cells were washed three times with PBS, and ATP levels in the cells were detected by ATP Assay Kit (Beyotime, China).

2.15. Mitochondrial membrane potential and LPO evaluation

LLC cells were inoculated in a confocal dish (3×10^5 cells/dish) and cultured for 24 h. Then cells were treated and grouped Control, FP, FP + Fer-1 and BPP. After 6 h, the cells were stained by JC-1 assay kit and C11-BODIPY 581/591 according to the manufacturer's protocols. The mitochondrial membrane potential and LPO were visualized by CLSM.

2.16. GSH detection

LLC cells were inoculated in the 6-well plates. Then, different concentrations of FP were added and incubated for 24 h, respectively. The GSH content was detected using the GSH detection kit (Beyotime, China).

2.17. Western blot

LLC cells were cultured as described in **Intracellular ATP Level Evaluation** and divided into different treatment groups. Using a solution containing protease with a phosphatase inhibitor and by following the manufacturer protocol, the total proteins were then extracted after the cells were lysed. Subsequently, the total protein was quantified using a BCA protein kit (Aladdin, China). The protein was analyzed using SDS-PAGE and transferred to a PVDF membrane for imaging. After being sealed with 5 % skim milk, it was sequentially incubated with HSP70, GPX4, GAPDH antibody (1:1000), HRP-labeled goat anti-rabbit secondary antibody (1:5000).

2.18. Hemolysis test

Mouse blood was centrifuged and washed to obtain red blood cells (RBCs) and suspended in PBS. FP was added to the erythrocyte suspension at various concentrations. Incubated at 37 °C for 3 h, centrifuged, and take photos. The hemolysis rate was determined and calculated.

2.19. MRI experiment

For *in vitro* MRI, LLC cells treated by different concentrations of FP were scanned by MR to acquire T2 MR images. For *in vivo* MRI, FP was injected into mice via vein, and the MRI effects at different time points were evaluated by a 9.4T MRI instrument. MRI scanning was performed by a 9.4T Bruker animal scanner (Bruker BioSpec 94/30). The gradient system allowed a maximal gradient strength of 660 mT/m with a slew rate of 4570 (T/m)/s. A series of scout images were acquired in the coronal view and the axial view of the tumor before each scanning session. The T2-weighted imaging parameters were as follows: TE = 33 ms, TR = 2500 ms, excitation angle = 90°, field of view = 3.6×3.0 cm^2, matrix size = 256×256, slice thickness = 0.8 mm, and number of repetitions per slice = 18.

2.20. In vivo tumor inhibition study

LLC cells were dispersed into a serum-free medium (1×10^7 cells/mL) and 100 μL was injected subcutaneously via the right side to establish a hormonal C57BL/6 mouse model. After the tumor reached an initial size of approximately 100 mm^3, the mice were randomly divided into PBS, PBS + NIR, BPP, FP, BPP + NIR and FP + NIR with 5 mice in each group. NIR irradiation was performed in the NIR group (1.5 W/cm^2, 5 min). After 13 days of measurement, the tumors were extracted, weighed, and photographed. Tumor volume (mm^3) = (length) × $(width)^2/2$.

2.21. In vivo biodistribution imaging

The LLCs-tumor-bearing mice were constructed subcutaneously on the right side of C57BL/6 mice (1×10^6 per mouse). FP-Cy5.5 was then injected intravenously into the mice. The fluorescence images were recorded at various time points (0 h, 1 h, 2 h, 4 h, 6 h) by an IVIS imaging system. Finally, all tumors and major tissues were excised and imaged after 6 h administration.

2.22. In vivo infrared thermal imaging

The LLCs-tumor-bearing mice were constructed subcutaneously on the right side of C57BL/6 mice; PBS, FP and BPP were then injected intravenously into the mice, respectively. After 2 h, tumors were exposed to an 808 nm laser (1.5 W/cm^2). The thermal images were obtained by using an infrared thermal camera.

2.23. Biosafety assessment

For histopathological analyses of major organs, the mice were sacrificed after the treatment to collect the major organs (brain, heart, liver, spleen, lung, and kidney). The tissue samples were stained with H&E. And to collect the blood for serum biochemistry assay of indicators.

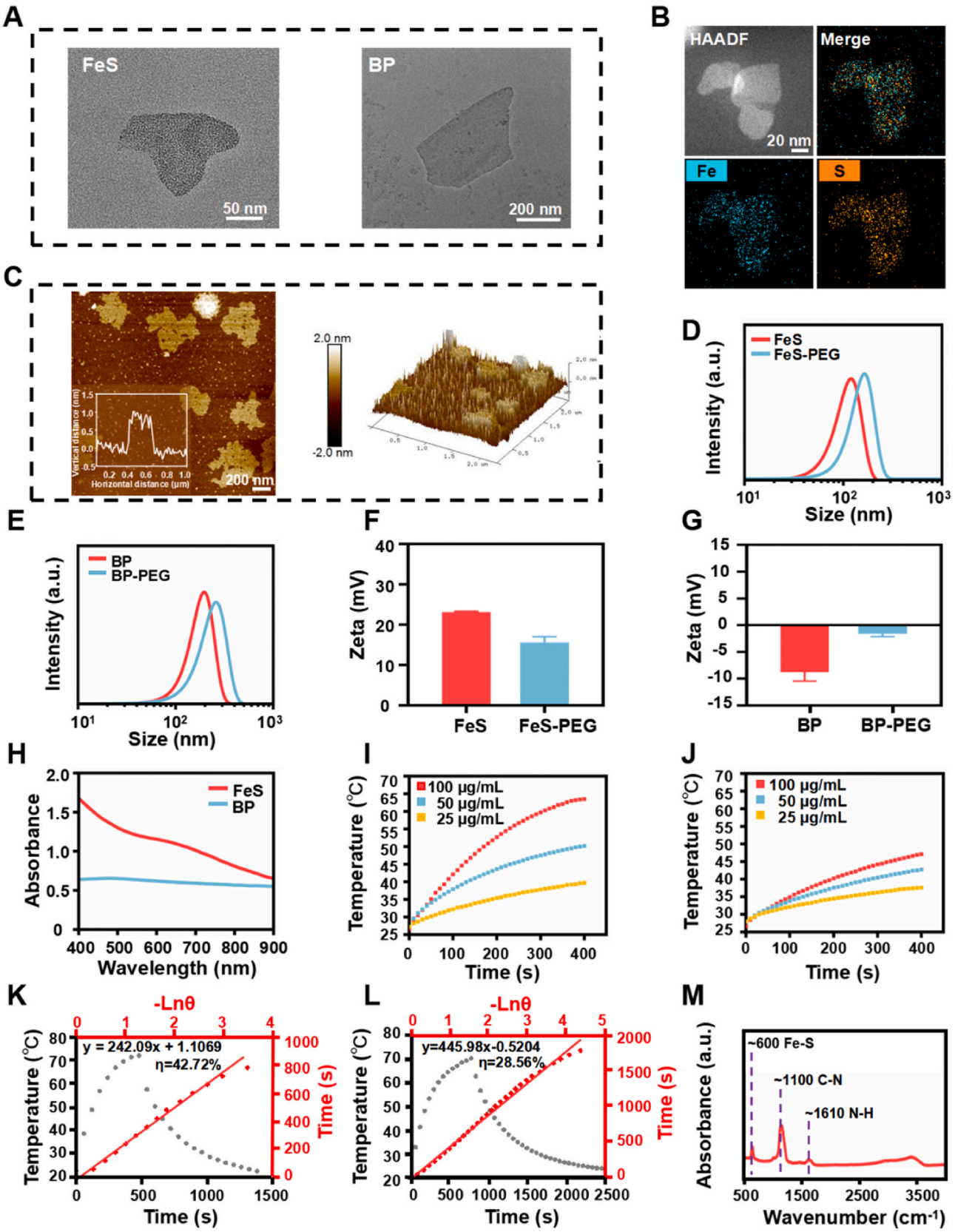

Fig. 1. Synthesis and characterization analyses. (A) TEM images of FeS and BP. (B) Elemental mapping of FeS. (C) Typical AFM image of FeS and the statistical thickness. (D) Hydrodynamic sizes of FeS and FP, and (E) BP and BPP. (F) ζ potential analysis of FeS and FP, and (G) BP and BPP. (H) UV–vis spectra of FeS and BP (80 μg/mL). (I) Photothermal-conversion heating curves under NIR laser irradiation with different concentrations of FeS and (J) BP. (K) Calculation of the PCE at 808 nm laser irradiation of FeS and (L) BP. (M) FTIR spectrum of FeS. Laser irradiation at 808 nm, 1.5 W/cm^2.

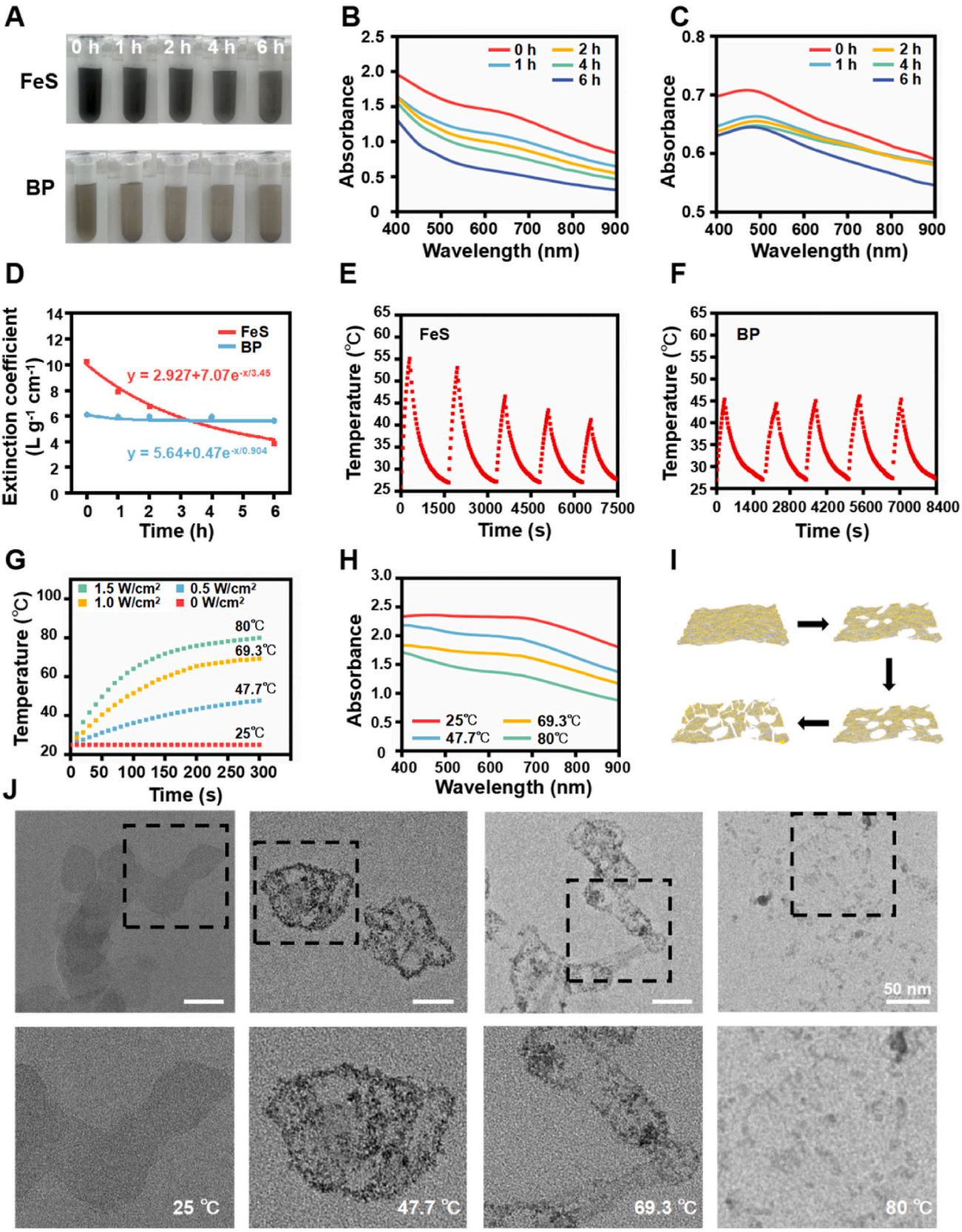

Fig. 2. Biodegradation performance analysis. (A) Photographs, (B) absorbance spectra of FeS and (C) BP (100 μg/mL) in varied degradation durations, and (D) the corresponding extinction coefficient. (E) Photothermal-conversion heating curves with 5 times NIR irradiation cycle of FeS and (F) BP. (G) Photothermal-conversion heating curves (5 min) of FeS aqueous solutions (150 μg/mL) showing varied photothermal-conversion temperatures. (H) Absorbance spectra, (I) the corresponding schematic diagram, and (J) TEM images with different magnifications for FeS degradation (150 μg/mL) at the corresponding temperatures by photothermal treatment.

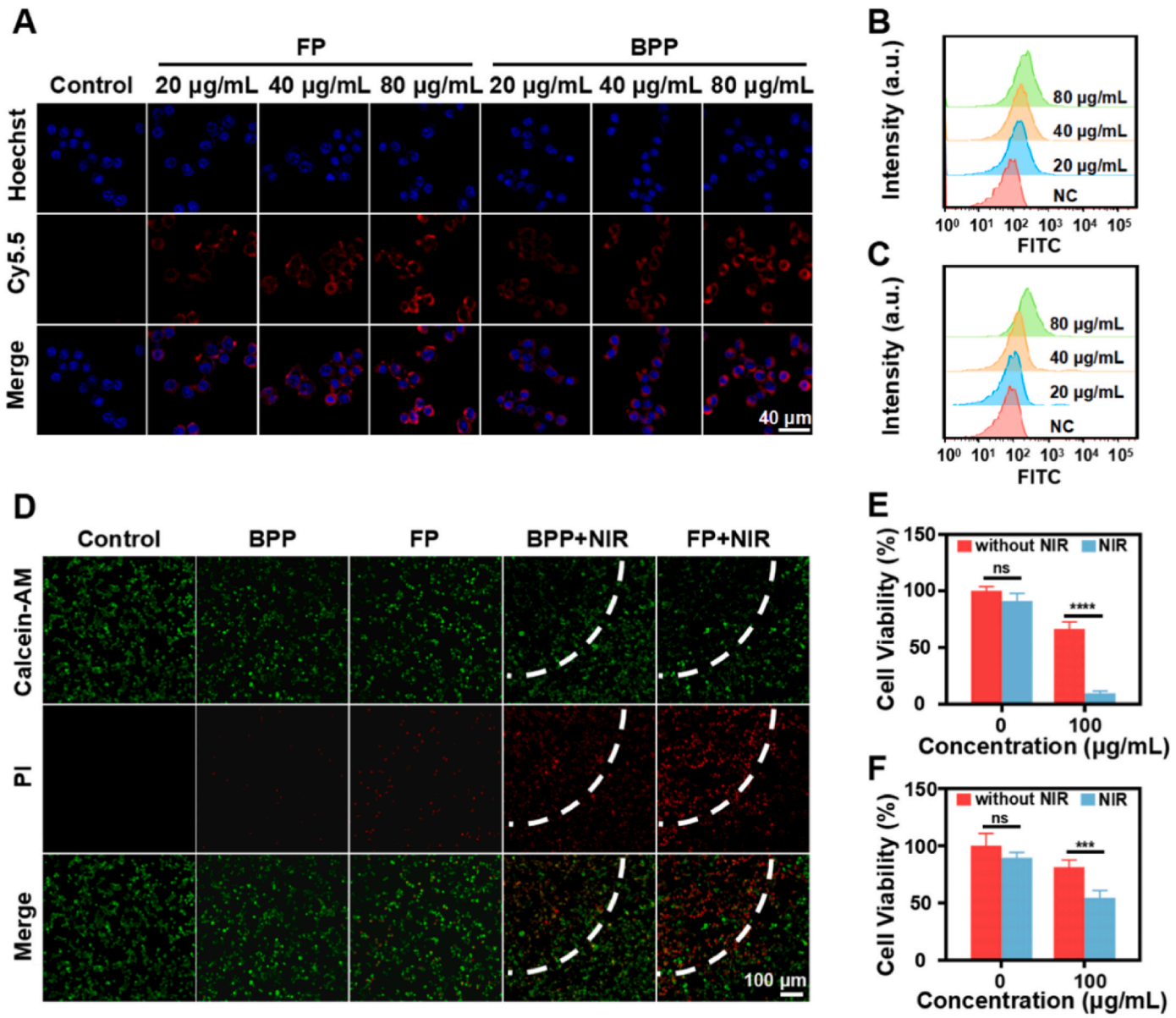

Fig. 3. ***In vitro*** **evaluation of antitumor properties.** (A) CLSM images of LLC cells internalization of FP and BPP with increasing dose. (B) FCM analysis of LLC cells internalization of FP and (C) BPP with increasing dose. (D) Fluorescent images of living and dead cells with different treatments by co-staining with Calcein-AM and PI. The white dotted line represents the boundary of the NIR. (E) Cell viabilities of LLC cells with or without NIR irradiation by FP and (F) BPP. Laser irradiation at 808 nm, 1.5 W/cm^2. (ns indicates no statistically significant difference, ***P < 0.001, ****P < 0.0001.)

2.24. Statistical analysis

All statistical data were analyzed using GraphPad Prism 8.0 software, and the results were expressed as mean ± standard deviation (SD). Comparisons between two groups were assessed using an unpaired two-tailed *t*-test. A p-value less than 0.05 ($P < 0.05$) was considered statistically significant, specifically with ns = non-significant, *p < 0.05, **p < 0.01, ***p < 0.001, and ****p < 0.0001.

3. Results and discussion

3.1. Preparation and characterization of the FeS-PEG and BP-PEG nanosheets

The detailed synthesis of the prepared FeS-PEG is illustrated in Scheme 1A. First, the ammonium iron (II) sulfate hexahydrate and thioacetamide were thoroughly stirred in ethylene glycol, followed by a reaction in an autoclave at 200 °C for 24 h resulting in the formation of FeS NSs. Then, polyethylene glycol (PEG) was functionalized onto the FeS NSs surface to enhance its biocompatibility. The TEM images (Fig. 1A) revealed that FeS exhibited a sheet morphology with uniform particle size and good dispersion, measuring approximately 100–150 nm. The atomic force microscope (AFM) demonstrated a thickness of about 1.5 nm (Fig. 1C). In contrast, BP displayed a larger and thicker lamellar morphology (Fig. 1A). Furthermore, elemental mapping results confirmed the presence of Fe and S elements in the FeS NSs as expected (Fig. 1B). Dynamic light scattering (DLS) measurement showed that the relative hydrodynamic size of FeS-PEG (abbreviated as FP) was slightly larger than that of FeS NSs (Fig. 1D), indicating the successful modification of PEG. Similarly, BP-PEG (abbreviated as BPP) was larger than bare BP NSs (Fig. 1E). The synthesized FeS NSs were concluded to be significantly thinner and smaller than both the commercial BP NSs used

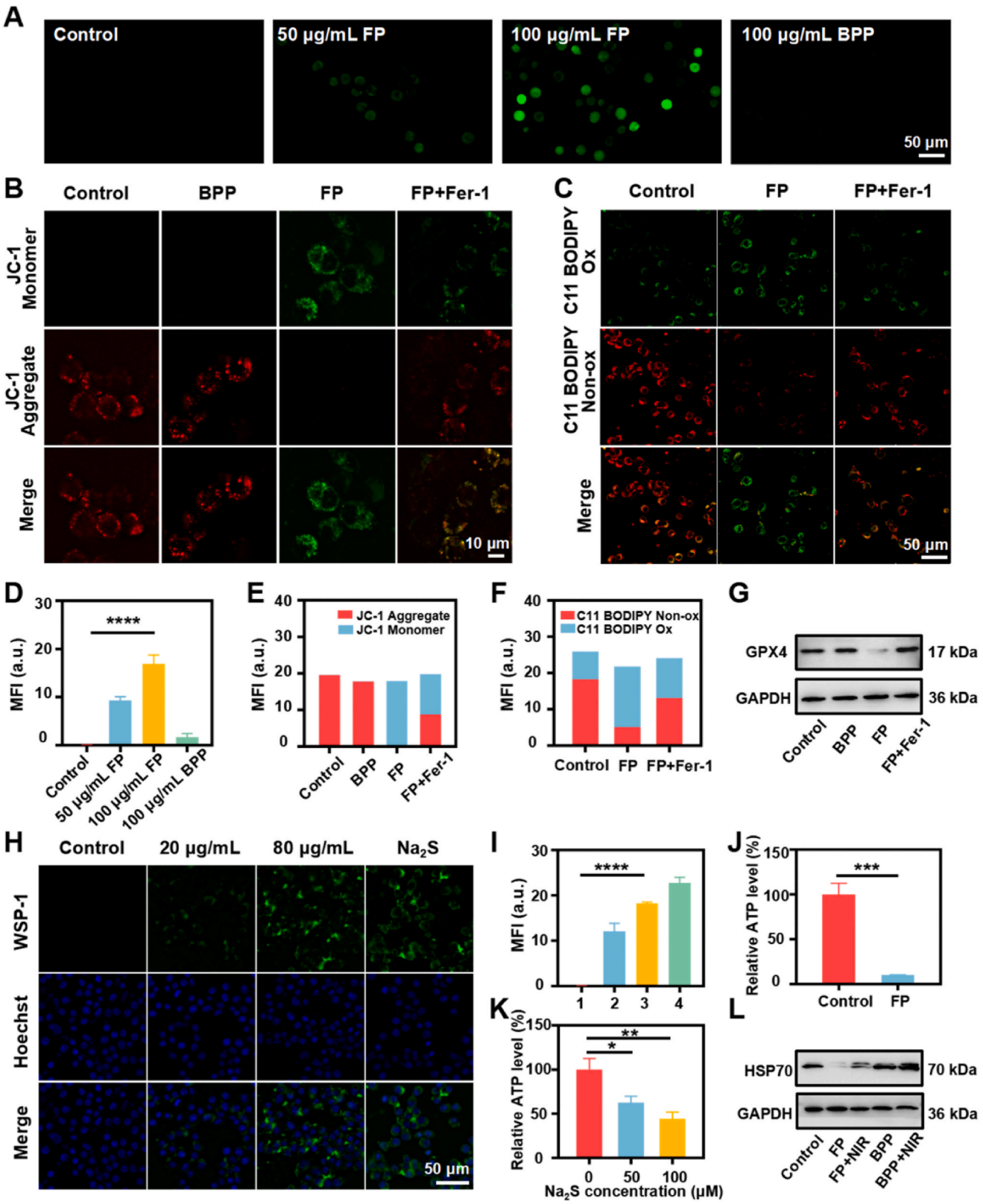

Fig. 4. Inducing-ferroptosis and intracellular H_2S-modulating antitumor mechanism. (A) CLSM images of DCFH-DA (for ROS) of LLC cells after different treatments. (B) CLSM observations of JC-1 probe-stained LLC cells with various treatments. (C) Intracellular LPO detection using C11-BODIPY 581/591 probe. Quantification of mean fluorescence intensity (MFI) for (D) DCF, (E) JC-1 and (F) C11-BODIPY. (G) Western blots of GPX4 with different treatments. (H) Fluorescence images of LLC cells treated by FP with increasing dose and Na_2S and WSP-1 probe and (I) the corresponding MFI (1: Control; 2: 20 μg/mL FP; 3: 80 μg/mL FP; 4: Na_2S). (J) Intracellular ATP levels of LLC cells after FP treatment. (K) Intracellular ATP levels of LLC cells after Na_2S treatment. (L) Western blots of HSP70 in LLC cells with different treatments. (*p < 0.05, **P < 0.01, ***P < 0.001, ****P < 0.0001.)

in this study (bought from XFNANO, with a thickness of 1–10 layers) and the previously reported BP NSs (Supporting Information, Table 1). Due to the presence of the abundant amine groups, FeS NSs showed a positive charge of approximately +23 mV. While the BP NSs had a negative charge of −8.8 mV. Upon modification of PEG, the absolute potentials values of both FeS NSs and BP NSs decreased (Fig. 1F and G). UV–vis spectra revealed that FeS NSs displayed higher absorption at 808 nm compared to BP NSs (Fig. 1H), which encourages to further explore and compare their photothermal properties. Fourier transform infrared (FTIR) spectra highlighted the respective characteristic chemical bonds of them (Fig. 1M and Fig. S1). The XPS analysis confirmed the presence of Fe, S, O, and N elements. Raman spectroscopy was further analyzed. The peaks at 280 cm^{-1} and 214 cm^{-1} are assigned to the symmetric and asymmetric stretching vibration of Fe-S, respectively (Fig. S2). Above results confirmed the successful synthesis of FeS NSs. The optical absorption spectra acquired on FeS NSs exhibited an intense absorption at 808 nm, which was higher than that of BP NSs. Although both materials are potential photothermal agents, FeS NSs exhibit superior photothermal performance. FeS and BP displayed a temperature increase with increasing concentration at the same 808 nm laser power (1.5 W/cm^2) (Fig. 1I and J). After the same duration and intensity of 808 nm laser radiation, FeS NSs rose to a higher temperature than BP NSs. The temperature of 100 μg/mL FeS elevated to almost 60 °C in 5 min while BP was less than 45 °C. The PCE of FeS NSs was calculated to be 42.72 %, surpassing that of BP NSs at 28.56 % (Fig. 1K and L). Therefore, compared to BP, FeS NSs may serve as a more effective photothermal agent for potential PTT applications.

3.2. *In vitro biodegradability of FeS/BP and photothermally accelerated degradation of FeS nanosheets*

The degradation performance of 2D nanomaterials remains a significant challenge for their clinical translations [29]. Therefore, investigating degradation characteristics of FeS/BP under ambient conditions is crucial for their future biomedical applications. To evaluate the biodegradability of FeS and BP NSs, they were dispersed in phosphate buffer saline (PBS) and exposed to the air at room temperature for 6 h. Subsequently, their optical/spectroscopic properties and morphology changes were analyzed at different time points (0, 1, 2, 4 and 6 h). The color of the FeS NSs suspension gradually weakened over time, attributed to its inherent strong reduction and degradation behavior (Fig. 2A and Fig. S3). In contrast, BP NSs showed a slight lightning of color during the same time frame. The corresponding UV–vis absorption spectra of FeS NSs suspension displayed a significant decrease in absorbance intensity as the dispersion time increased, while BP NSs remained stable (Fig. 2B, C, D). Accordingly, it is indicated that FeS NSs exhibit a prominent degradation capacity over BP NSs. To evaluate the acid-responsive degradation of FeS and BP NSs, they were dispersed in PBS of pH 7.4 and 5.5 and exposed to the air at room temperature for 6 h (Fig. S4). The color of FeS NSs suspensions weakened over time, which was particularly notable in PBS of pH 5.5, suggesting a strong reduction and acid-responsive degradation behavior. In contrast, BP NSs in PBS of pH 7.4 and 5.5 showed a slight lightning of color during the same time frame. The corresponding UV–vis absorption spectra of FeS NSs suspension displayed a decrease in absorbance intensity as the dispersion time increased, and the decrease in absorbance was more significant when dispersed in PBS of pH 5.5. The same degradation trend was observed in simulated body fluids and simulated acidic TME (Fig. S5). The results showed that FeS NSs have acid-responsive degradation properties. BP was relatively stable, but acidic environments also enhanced BP degradation.

Moreover, significant temperature changes of FeS could be observed during the 5 times on/off laser exposure cycles, and BP barely changed (Fig. 2E and F). The findings suggest that while BP demonstrated photothermal stability, FeS exhibited excellent photothermal-enhanced degradability. In other words, FeS can degrade *in vivo* after effectively performing its role in photothermal conversion. The experimental evaluations were conducted to investigate the photothermal-induced biodegradation behavior of FeS NSs. The FeS NSs-dispersed aqueous suspensions were exposed to 808 nm laser irradiation for 5 min at varying power densities to achieve different temperature elevations (25, 47.7, 69.3, and 80 °C) (Fig. 2G). The absorbance intensity of the FeS NSs in water decreased as temperature elevated (Fig. 2H). TEM observation results further supported this photothermal-enhanced biodegradation process. The FeS NSs show a significant change in morphology with the increasing treatment temperature (Fig. 2I and J). Specifically, at 47.7 °C, the lamellar morphology became porous and fragmented. Subsequently, when the temperature was raised to 69.3 °C, there was obvious change in morphology characterized by a gradual cleavage of FeS into smaller nanofragments due to intense oxidation on the NSs. Finally, at 80 °C, the majority of FeS NSs were converted into highly dispersed 2D fragmented structures. These findings underscore a temperature-dependent degradation behavior of the synthesized FeS NSs.

3.3. *Cellular uptake performance and antitumor effect of FeS-PEG and BP-PEG nanosheets in vitro*

Flow cytometry (FCM) analysis and confocal laser scanning microscopy (CLSM) were used to analyze the cellular uptake of FP and BPP (Fig. 3A, B, C and Figure S6). LLC cells displayed obvious dose-dependent fluorescence intensity enhancement, indicating that both FP and BPP can be effectively internalized by LLC cells with dose dependence. In order to explore optimal laser power densities conditions for treatment, the MTT experiments under different power conditions were carried out (Fig. S7). The results showed that the photothermal killing ability of FP on cells became stronger with higher laser power, and the killing effect of the 1.5 W/cm^2 condition was far more prominent than that of 1 W/cm^2, and not much weaker than that of 2 W/cm^2. For the consideration of therapeutic effect and safe dose for laser exposure, the 1.5 W/cm^2 power condition was chosen as the optimal one. The cytotoxicity of FP and BPP were determined via MTT assay. The cell survival rate decreased with the addition of FP, and the cell survival rate decreased sharply under NIR condition, with only 10 % of cells surviving at 100 μg/mL, reflecting the excellent PCE of FeS (Fig. 3E). BPP itself was not significantly toxic to cells, and the cell survival rate dropped to 55 % under NIR conditions, which was weaker than the PTT killing effect of FP (Fig. 3F). The results from Calcein-AM/PI staining were consistent with those obtained from the MTT assay. Lewis lung carcinoma (LLC) cells with both FP and NIR treatment displayed more cell death than those with only FP treatment (Fig. 3D and Fig. S8). Additionally, the combination of FP and NIR resulted in significantly more cell death compared to the combination of BPP and NIR. The biocompatibility experiment was conducted with HUVEC cells as a model, and the cell survival rate of them with FP or BPP treatment was above 81 % in the concentration range of the administered drug, which indicated that it had good cell compatibility (Figs. S9 and 10). The above results confirmed both FP and BPP had PTT effect, but FP was more effective. Therefore, FP can be a better agent for efficient tumor therapy. What's more, FP itself can kill tumor cells without NIR.

3.4. *FeS-PEG enhances its inducing-ferroptosis ability in tumor cells*

Subsequently, intracellular hydroxyl radicals (·OH) production was investigated using DCFH-DA as a probe (Fig. 4A and D). The strongest green fluorescence of DCF was observed in the high concentration FP group, indicating the Fe^{2+}-catalyzed Fenton reaction process promoted the production of ·OH [30]. H_2S, generated by the decomposition of FeS under acidic conditions, can interact with mitochondrial proteins, and ·OH induces peroxidation of mitochondrial lipids, leading to damage in the electron transport chain and alterations in the mitochondrial membrane potential. Mitochondrial function was assessed using the JC-1 probe (Fig. 4B and E). The results showed that, after FP treatment,

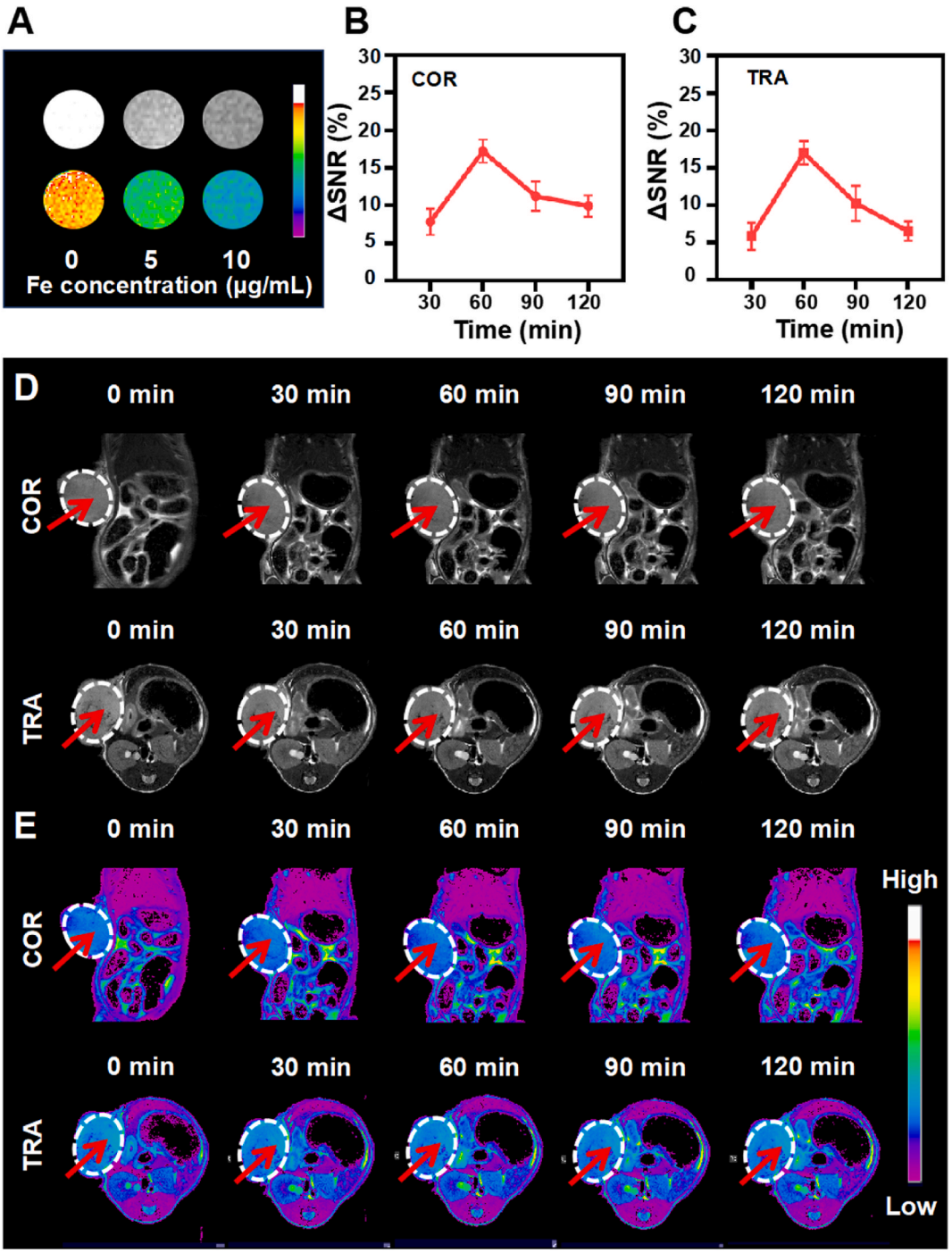

Fig. 5. MRI performance analysis. (A) *In vitro* T2 MR gray images and corresponding pseudocolor images of FP in LLC cells. (D) T2-weighted coronal images and transverse images of mice acquired at different time points post-injection of FP with a Fe dose of 4 mg kg^{-1} and (E) the corresponding pseudocolor images as well as the corresponding ΔSNR (B and C).

the green fluorescence representing JC-1 monomer was improved, while the red fluorescence representing JC-1 aggregates was significantly decreased. This indicates that the H_2S and •OH produced by FP led to a reduction in mitochondrial membrane potential, resulting in mitochondrial damage. In addition, the level of lipid peroxidation (LPO) and glutathione (GSH) in LLC cells were analyzed respectively (Fig. 4C and F and Fig. S11). The results showed that LPO levels increased and GSH levels decreased with FP treatment, suggesting that FP could induce oxidative stress in cells. The massive accumulation of LPO and reduction of GSH both contribute to subsequent ferroptosis, as evidenced by decreased expression of glutathione peroxidase 4 (GPX4) (Fig. 4G and Fig. S12). Ferrostatin-1 (Fer-1), an active ferroptosis inhibitor, could both protect against damage to mitochondrial by FP and reduce the levels of LPO.

3.5. *Investigation of the intracellular H_2S-modulating performance of FeS-PEG nanosheets*

As reported, H_2S can impede the oxidative phosphorylation process in the mitochondrial respiratory chain by reducing the activation of cytochrome C oxidase (COX IV), disrupting energy metabolism, and ultimately leading to cellular dysfunction and death [31]. The

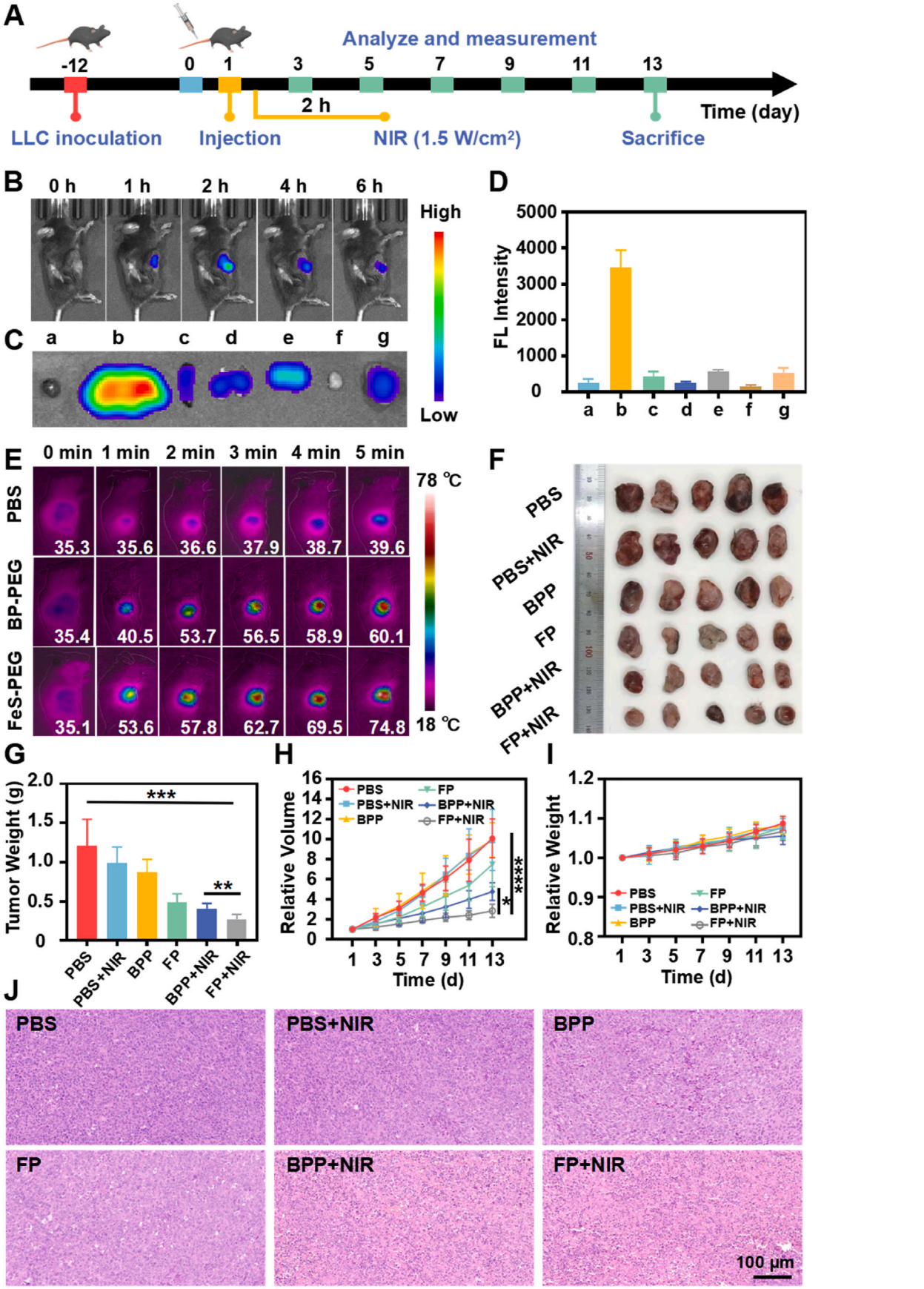

(caption on next page)

Fig. 6. *In vivo* biodistribution analysis and cancer therapy. (A) Schematic illustration of tumor model establishment and therapy process. (B) *In vivo* fluorescence images of LLCs-tumor-bearing mice after the injection of Cy5.5-labeled FP at different time intervals. (C) *Ex vivo* fluorescence images of major tissues at 6 h post-injection of Cy5.5-labeled FP, and (D) the quantification of fluorescence intensity of various tissues (a: Heart; b: Liver; c: Spleen; d: Lung; e: kidney; f: Muscle; g: Tumor). (E) Infrared thermal images and the corresponding temperature elevations at the tumor regions of LLCs-tumor-bearing mice with different treatment. (F) The photographs and (G) eventual average weights of tumors after different treatments for 13 days. (H) Relative tumor volume curves and (I) relative body weight curves of LLCs-tumor-bearing mice under distinct treatments during 13 days. (J) H&E staining of tumor tissues dissected from the mice in various groups. Laser irradiation at 808 nm, 1.5 W/cm^2. (*P < 0.05, **P < 0.01, ***P < 0.001, ****P < 0.0001.)

production of H_2S was demonstrated in Fig. 4K after the cells was treated by Na_2S with increasing dose, clearly illustrates the inhibitory effect of H_2S on ATP levels. The H_2S level in LLC cells was assessed using the WSP-1 probe, the results indicating that the green fluorescence intensity gradually increased after FP treatment (Fig. 4H and I), suggesting the H_2S level within LLC cells rose. This increase is attributed to that FeS with pH-response can generate Fe^{2+} and H_2S within the acidic tumor microenvironment. Therefore, ATP production is significantly reduced after FP treatment (Fig. 4J). By inhibiting the synthesis of heat shock proteins (HSPs) in the process of PTT, the heat resistance of tumor cells can be reduced, thereby enhancing the PTT effect [32]. Hence, it is essential to explore whether the down-regulation of ATP can lead to a decrease in HSPs expression. Western blot results showed a remarkable decrease in HSP70 levels in FP-treated LLC cells, as well as in the FP with NIR group compared to the control group (Fig. 4L and Fig. S13). However, LLC cells treated by the conventional photothermal agent BP exhibited heat generation under NIR conditions, prompting the synthesis of HSPs to protect the cells and potentially impact the effectiveness of PTT. These findings suggest that FP can suppress the production of ATP by generating H_2S and further reduce the expression of HSPs at the cellular level. An in-depth study on the specific mechanism of FP inhibiting mitochondrial respiration in cell was conducted (Fig. S14). Western blot results showed significant differences between the control, BPP and FP groups for COX IV. This suggests that the inhibition of mitochondrial respiration by FP is mainly attributed to the suppression of COX IV expression.

3.6. Evaluation of MRI performance of FeS-PEG in vivo

The performance of the developed FP as contrast agents for MR imaging was investigated *in vitro*. T2-weighted MR images of LLC cells treated by FP exhibited dose-dependent contrast enhancement (Fig. 5A), which indicated that FP can be effectively internalized by LLC cells. The excellent *in vitro* MRI performance of FP encouraged us to further explore the MRI performance of FP *in vivo*. As shown in MR images, significantly enhanced negative signals at the tumor site were observed at 60 min post-injection (Fig. 5D and E). The relative signal-to-noise ratio (ΔSNR) of the FP group reached 17.01 % (axial) and 17.24 % (coronal), respectively (Fig. 5B and C). Hence, FP could serve as a potential MRI nanoplatform to enhance magnetic resonance contrast, which provide a highly sensitive imaging evidence for precise tumor diagnosis, and potentially guide subsequent anti-tumor therapy.

3.7. Investigation of FeS-PEG's biodistribution, anti-tumor efficacy, and biosafety in vivo

Next, fluorescence imaging was performed *in vivo* to examine the distribution of FP in living body of mice (Fig. 6B). The results showed that fluorescence levels peaked approximately 2 h' post-injection, with accumulation of FP at tumor site reaching a maximum before gradually diminishing. Upon dissection, FP showed strong fluorescence in the liver, which could be valid evidence that FP is mainly metabolized through the liver (Fig. 6C and D). Building upon the promising *in vitro* laser absorbance, photothermal-conversion capabilities and *in vivo* accumulation efficiency of FP, the *in vivo* PTT experiments were further performed on LLCs-tumor-bearing mice. Following irradiation with an 808 nm laser, mice injected with FP via the tail vein exhibited a more significant temperature increase at tumor sites compared to BPP-injected mice, indicating that FP possessed superior photothermal properties and could effectively induce PTT effect on tumor tissues (Fig. 6E).

For a more comprehensive evaluation and comparison on FeS and BP in anti-tumor efficacy, the LLCs-tumor-bearing C57BL/6 mice were randomly divided into six groups: PBS, PBS + NIR, BPP, FP, BPP + NIR, FP + NIR. The therapeutic process was monitored for 13days post-treatment (Fig. 6A). Results showed that the tumor volume continued to increase in the PBS group, PBS + NIR group and BPP group, while the tumor volume in the FP group was inhibited to a certain extent. Remarkably, the tumor volume in the BPP + NIR group and FP + NIR group was significantly suppressed, with FP + NIR group showing the most pronounced effect (Fig. 6F–H). H&E staining results showed the most extensive damage of tumor tissues of FP + NIR group (Fig. 6J). In consistent with *in vitro* therapeutic findings, *in vivo* experiments confirmed that FP effectively induced ferroptosis and apoptosis in tumor cells. Consequently, the combination of FP and NIR resulted in a synergistic ferroptosis-PTT effect, leading to a highly effective anti-tumor therapy that surpassed the efficacy of BPP combined with NIR.

The nanosheet exhibited excellent degradability and *in vivo* clearance of FeS, demonstrating favorable biosafety characteristics essential for an ideal 2D nanomaterial. Throughout the study, the body weights of mice increased steadily, indicating the good biosafety profile of these NPs (Fig. 6I). After 13 days, all mice were euthanized, and blood along with major organs were collected. Serum biochemical indices (ALT, AST, UREA, CREA, CK and LDH) of major organs were measured to evaluate functional toxicities. As is shown in Fig. 7A and Fig. S15, all groups displayed similar values to those of PBS group, and all indicators fell within the normal reference range. The serum inflammatory factors in PBS group and FP treatment group were detected. There was no significant difference in the level of inflammatory factors between the FP group and the PBS group, which indicated that FP did not cause significant inflammatory reactions of mice (Fig. S16). In addition, hemolysis test also showed that FP had a relatively low hemolysis activity (Fig. S17), indicating FP had good blood compatibility. Furthermore, representative H&E staining images indicated no significant variations in the main organs of mice treated with FP (Fig. 7B). The distribution and the metabolic behavior of FP in mice showed that with the extension of time, Fe content in various organs showed obvious decrease, which indicated that FeS metabolized at a faster rate and could be effectively excreted from the body, thus reducing the accumulation of Fe in the body with a good safety (Fig. S18). The half-life of FP during blood circulation was investigated by collecting blood at different time points post-injection. The obtained data were fitted to a time-dependent concentration curve (Fig. S19). It was found that the concentration of the iron ions decreased sharply within 12 h, and the half-life of FP was calculated to be 5.61 h. Overall, the combination of FP with NIR exhibited the most effective tumor growth inhibition with expected *in vivo* compatibility, indicating its potential for clinical translation. We believe that over time, emerging sulfide nanomaterials will extend their applicability into other non-tumor diseases [33].

4. Conclusions

To sum up, a novel type of 2D FeS nanosheets with prominent biodegradability has been designed and synthesized via a one-step solvothermal reaction. Given its excellent properties including high PCE, rapid degradation, enhanced T2 MRI and the ability to induce

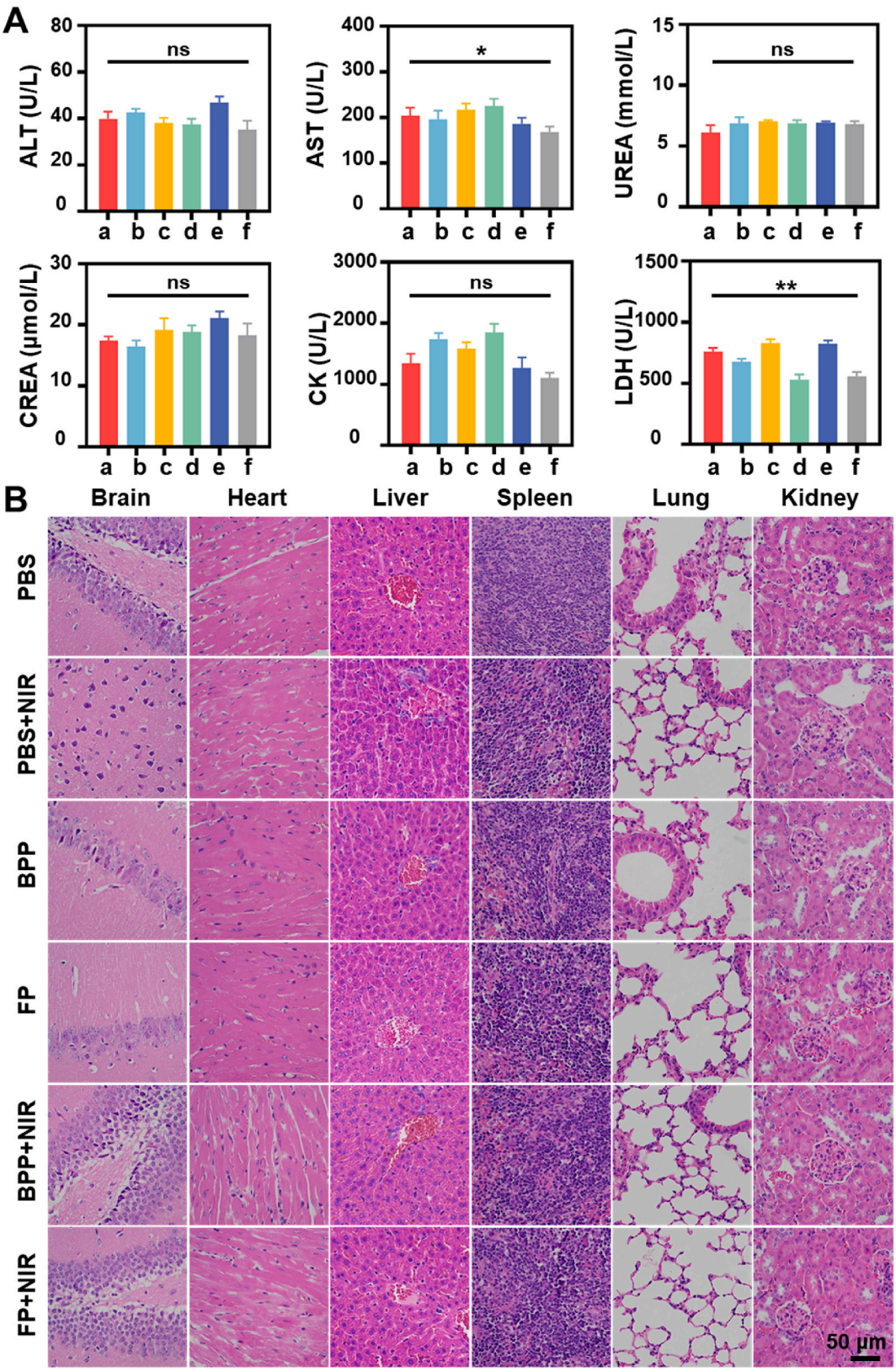

Fig. 7. Biocompatibility and biosafety evaluation. (A) Serum biochemistry assay of indicators and (B) H&E staining of the major organs after various treatments. (a: PBS; b: PBS + NIR; c: BP; d: FP; e: BPP + NIR; f: FP + NIR). (ns indicates no statistically significant difference, *P < 0.05, **P < 0.01.)

ferroptosis, it is considered a promising candidate to succeed BP in the field of 2D nanomaterials for MR imaging-guided synergetic ferroptosis-PTT tumor therapy. FeS demonstrates effective PTT tumor elimination owing to their high PCE and ability to generate Fe^{2+} and H_2S within the acidic tumor microenvironment. (I) The released Fe^{2+} exhibits potent POD-like activity, effectively inducing tumor cell ferroptosis. (II) H_2S plays a key role in inhibiting mitochondrial respiration and ATP production in tumor cells, (III) consequently decreasing HSP70 expression, (IV) which can reduce the resistance of tumor cells to PTT and enhancing PTT effect. As a result, FeS emerges as a superior candidate for 2D photothermal nanomaterials in cancer theranostic applications compared to BP.

Data availability statement

The data that support the findings of this study are available from the corresponding author upon reasonable request.

Ethics approval and consent to participate

The animal experiments were approved by the Experimental Animal Care Ethics Committee of Shandong First Medical University (Approval No. SDTHEC2023003137). All animal experiments were performed in accordance with relevant ethical regulations.

CRediT authorship contribution statement

Yuan Gao: Writing – review & editing, Writing – original draft, Project administration, Data curation. **Mengyao Mu:** Writing – original draft, Project administration, Formal analysis, Data curation. **Yiju Wei:** Writing – review & editing, Project administration, Methodology, Investigation. **Bowen Yan:** Writing – original draft, Methodology, Data curation. **Hui Liu:** Project administration, Formal analysis, Data curation. **Kai Guo:** Methodology, Data curation. **Mengmeng Zhang:** Writing – review & editing, Writing – original draft. **Xiaohui Dai:** Writing – review & editing, Writing – original draft. **Xiao Sun:** Writing – review & editing, Writing – original draft, Supervision, Conceptualization. **David Tai Leong:** Writing – review & editing, Writing – original draft, Supervision, Conceptualization.

Declaration of competing interest

David Tai Leong is an associate editor for Bioactive Materials and was not involved in the editorial review or the decision to publish this article. All authors declare that there are no competing interests.

Acknowledgments

This work was financially supported by the National Natural Science Foundation of China (82372031, 22104073), the Natural Science Foundation of Shandong (2022HWYQ-079, ZR2021QB119), the Taishan Scholar Foundation of Shandong Province (tsqn202408248), the Youth Innovation Science and Technology Program of Shandong Provincial Universities (2021KJ100), the Shandong Provincial Postdoctoral Innovation Project (SDCX-ZG-202400053, SDCX-ZG-202400029), the Incubation Foundation of Shandong Provincial Hospital (2023FY086), NUS Reimagine Grant (A-0009179-02-00 and A-0009179-03-00) and NUS NanoNASH Program (N-176-000-031-001).

Appendix A. Supplementary data

Supplementary data to this article can be found online at https://doi.org/10.1016/j.bioactmat.2024.09.035.

References

[1] L. Ding, M. Liang, C. Li, X. Ji, J. Zhang, W. Xie, R.L. Reis, F.-R. Li, S. Gu, Y. Wang, Design strategies of tumor-targeted delivery systems based on 2D nanomaterials, Small Methods 6 (11) (2022) 2200853.
[2] S. Shi, X. Li, Y. Zhang, H. Huang, J. Liu, J. Zhang, Z. Wang, H. Niu, Y. Zhang, Q. Mei, Ultrathin and biodegradable bismuth oxycarbonate nanosheets with massive oxygen vacancies for highly efficient tumor therapy, Small (2024) 2307974.
[3] N. Ni, X. Zhang, Y. Ma, J. Yuan, D. Wang, G. Ma, J. Dong, X. Sun, Biodegradable two-dimensional nanomaterials for cancer theranostics, Coord. Chem. Rev. 458 (2022) 214415.
[4] L. Rochette, G. Dogon, E. Rigal, M. Zeller, Y. Cottin, C. Vergely, Lipid peroxidation and iron metabolism: two corner stones in the homeostasis control of ferroptosis, Int. J. Mol. Sci. 24 (1) (2022) 449.
[5] Z. Kan, K.X. Zhao, C. Jiang, D.Y. Liu, Y. Guo, L.Y. Liu, W.J. Wang, Z.Q. He, Z. F. Zhang, S.Y. Wang, Respiratory exposure to graphene oxide induces pulmonary fibrosis and organ damages in rats involving caspase-1/p38MAPK/TGF-β1 signaling pathways, Chemosphere 303 (2022) 135181.
[6] L.E. Sima, G. Chiritoiu, I. Negut, V. Grumezescu, S. Orobeti, C.V.A. Munteanu, F. Sima, E. Axente, Functionalized graphene oxide thin films for anti-tumor drug delivery to melanoma cells, Front. Chem. 8 (2020) 184.
[7] P. Wang, X. Wang, Q. Tang, H. Chen, Q. Zhang, H. Jiang, Z. Wang, Functionalized graphene oxide against U251 glioma cells and its molecular mechanism, Mater. Sci. Eng. C 116 (2020) 111187.
[8] J. Li, L.M. Guiney, J.R. Downing, X. Wang, C.H. Chang, J. Jiang, Q. Liu, X. Liu, K. C. Mei, Y.P. Liao, T. Ma, H. Meng, M.C. Hersam, A.E. Nel, T. Xia, Dissolution of 2D molybdenum disulfide generates differential toxicity among liver cell types compared to non-toxic 2D boron nitride effects, Small 17 (25) (2021) e2101084.
[9] M. Domanico, A. Fukuto, L.M. Tran, J.M. Bustamante, P.C. Edwards, K. E. Pinkerton, S.M. Thomasy, L.S. Van Winkle, Cytotoxicity of 2D engineered nanomaterials in pulmonary and corneal epithelium, NanoImpact 26 (2022) 100404.
[10] X. Liu, K. Chen, X. Li, Q. Xu, J. Weng, J. Xu, Electron matters: recent advances in passivation and applications of black phosphorus, Adv. Mater. 33 (50) (2021) e2005924.
[11] H. Zhu, L. Gou, C. Li, X. Fu, Y. Weng, L. Chen, B. Fang, L. Shuai, G. Liao, Dual interfacial electric fields in black phosphorus/MXene/MBene enhance broad-spectrum carrier migration efficiency of photocatalytic devices, Device 2 (3) (2024) 100283.
[12] H. Jiang, Y. He, J. Zhao, R. Chang, H. He, T. Li, X. Zhang, B. Shu, W. Zhang, H. Wang, J. Liu, S. Zhang, Y. Zhao, Immunostimulant nanomodulator boosts antitumor immune response in triple negative breast cancer by synergism of vessel normalization and photothermal therapy, Nano Res. 16 (8) (2023) 11149–11163.
[13] C. Zhao, J. Lin, Y. Cai, Y. Zhong, Y. Li, B. Zhou, Evaluation of stability and antitumor activity of two-dimensional black phosphorus modified with positively charged protein, Nanotechnology 34 (33) (2023) 335701.
[14] H. Lu, J. Wei, K. Liu, Z. Li, T. Xu, D. Yang, Q. Gao, H. Xiang, G. Li, Y. Chen, Radical-scavenging and subchondral bone-regenerating nanomedicine for osteoarthritis treatment, ACS Nano 17 (6) (2023) 6131–6146.
[15] S. Xiong, X. Chen, Y. Liu, T. Fan, Q. Wang, H. Zhang, T. Chen, Black phosphorus as a versatile nanoplatform: from unique properties to biomedical applications, J. Innovative Opt. Health Sci. 13 (5) (2020) 2030008.
[16] G.F. Liao, F. He, Q. Li, L. Zhong, R.Z. Zhao, H.N. Che, H.Y. Gao, B.Z. Fang, Emerging graphitic carbon nitride-based materials for biomedical applications, Prog. Mater. Sci. 112 (2020) 100666.
[17] F. Zeng, S. Nijiati, Y. Liu, Q. Yang, X. Liu, Q. Zhang, S. Chen, A. Su, H. Xiong, C. Shi, C. Cai, Z. Lin, X. Chen, Z. Zhou, Ferroptosis MRI for early detection of anticancer drug-induced acute cardiac/kidney injuries, Sci. Adv. 9 (10) (2023) eadd8539.
[18] G. Ma, X. Zhang, K. Zhao, S. Zhang, K. Ren, M. Mu, C. Wang, X. Wang, H. Liu, J. Dong, X. Sun, Polydopamine nanostructure-enhanced water interaction with pH-responsive manganese sulfide nanoclusters for tumor magnetic resonance contrast enhancement and synergistic ferroptosis-photothermal therapy, ACS Nano 18 (4) (2024) 3369–3381.
[19] L. Zhang, G. Oudeng, F.Q. Wen, G.F. Liao, Recent advances in near-infrared-II hollow nanoplatforms for photothermal-based cancer treatment, Biomater. Res. 26 (1) (2022) 61.
[20] Z. Mo, M. Qiu, K. Zhao, H. Hu, Q. Xu, J. Cao, Y. Luo, L. Liu, Z. Xu, C. Yi, Z. Xiong, G. Liao, S. Yang, Multifunctional phototheranostic nanoplatform based on polydopamine-manganese dioxide-IR780 iodide for effective magnetic resonance imaging-guided synergistic photodynamic/photothermal therapy, J. Colloid Interface Sci. 611 (2022) 193–204.
[21] S. Liang, G. Liao, W. Zhu, L. Zhang, Manganese-based hollow nanoplatforms for MR imaging-guided cancer therapies, Biomater. Res. 26 (1) (2022) 32.
[22] X. Chen, S. Teng, J. Li, X. Qiao, W. Zhao, Z. Xue, X. Shi, Y. Wang, W. Yang, T. Wang, Gadolinium (III)-Chelated deformable mesoporous organosilica nanoparticles as magnetic resonance imaging contrast agent, Adv. Mater. 35 (20) (2023) 2211578.
[23] H. Liu, M. Mu, Y. Hou, Y. Gong, C. Wang, G. Ma, K. Guo, L. Ma, X. Sun, A novel CRISPR/Cas9-Encapsulated biomimetic manganese sulfide nanourchins for targeted magnetic resonance contrast enhancement and self-enhanced chemodynamics-gene-immune synergistic tumor therapy, Adv. Funct. Mater. (2024) 2401370.
[24] S. Liu, Y. Jiang, P. Liu, Y. Yi, D. Hou, Y. Li, X. Liang, Y. Wang, Z. Li, J. He, H. Rong, D. Wang, J. Zhang, Single-Atom gadolinium nano-contrast agents with high

stability for tumor T1 magnetic resonance imaging, ACS Nano 17 (9) (2023) 8053–8063.
[25] W. Sun, C. Zhu, J. Song, S.-C. Ji, B.-P. Jiang, H. Liang, X.-C. Shen, Hydrogen sulfide gas amplified ROS cascade: FeS@GOx hybrid nanozyme designed for boosting tumor chemodynamic immunotherapy, Adv. Healthcare Mater. 12 (23) (2023) 2300385.
[26] G.F. Liao, L. Zhang, C.X. Li, S.Y. Liu, B.Z. Fang, H.M. Yang, Emerging carbon-supported single-atom catalysts for biomedical applications, Matter 5 (10) (2022) 3341–3374.
[27] X. Zhang, H. Ge, Y. Ma, L. Song, Y. Ma, G. Tian, L. Wang, Q. Meng, X. Sun, Engineered anti-cancer nanomedicine for synergistic ferroptosis-immunotherapy, Chem. Eng. J. 455 (2023) 140688.
[28] C. Xie, D. Cen, Z. Ren, Y. Wang, Y. Wu, X. Li, G. Han, X. Cai, FeS@BSA nanoclusters to enable H(2)S-amplified ROS-based therapy with MRI guidance, Adv. Sci. 7 (7) (2020) 1903512.
[29] Z. Chen, Y. Tian, J. Yang, F. Wu, S. Liu, W. Cao, W. Xu, T. Hu, D.J. Siegwart, H. Xiong, Modular design of biodegradable ionizable lipids for improved mRNA delivery and precise cancer metastasis delineation in vivo, J. Am. Chem. Soc. 145 (44) (2023) 24302–24314.
[30] Z.Z. Qin, M.J. Qiu, Q.Y. Zhang, S.L. Yang, G.F. Liao, Z.F. Xiong, Z.S. Xu, Development of copper vacancy defects in a silver-doped CuS nanoplatform for high-efficiency photothermal-chemodynamic synergistic antitumor therapy, J. Mater. Chem. B 9 (42) (2021) 8882–8896.
[31] J. Cheng, Y. Zhu, Y. Dai, L. Li, M. Zhang, D. Jin, M. Liu, J. Yu, W. Yu, D. Su, J. Zou, X. Chen, Y. Liu, Gas-mediated tumor energy remodeling for sensitizing mild photothermal therapy, Angew. Chem. Int. Ed. 62 (27) (2023) e202304312.
[32] G. Ma, Z. Liu, C. Zhu, H. Chen, R.T.K. Kwok, P. Zhang, B.Z. Tang, L. Cai, P. Gong, H (2) O(2) -responsive NIR-II AIE nanobomb for carbon monoxide boosting low-temperature photothermal therapy, Angew. Chem. Int. Ed. 61 (36) (2022) e202207213.
[33] M. Wang, H. Zhu, Y. Xue, Y. Duan, H. Tian, Q. Liu, Y. Zhang, Z. Li, X.J. Loh, E. Ye, G. Yin, X. Wang, X. Ding, D.T. Leong, Baiting bacteria with amino acidic and peptidic corona coated defect-engineered antimicrobial nanoclusters for optimized wound healing, Bioact. Mater. 42 (2024) 628–643.